

Performance Improvement of Full-Converter Wind Turbines Under Distorted Conditions

Andres E. Leon, *Member, IEEE*, and Jorge A. Solsona, *Senior Member, IEEE*

Abstract—This work presents a control strategy to improve the performance of full-converter wind turbines under distorted conditions, particularly with regards to the harmonic rejection capability under grid frequency variations. Resonant filters are often added to the grid-side converter control to achieve a proper operation against network disturbances. However, in weak power networks where frequency deviations are expected, these schemes can lose some performance since they are susceptible to grid frequency drifts. The proposed control structure allows us to adapt the grid frequency involved in different control blocks via a frequency-updating outer loop; thus, the control algorithm is tailored so that full-converter wind turbines inject a harmonic-free current even under severe harmonic distortions and frequency-varying conditions. This facilitates that wind farms overcome most network disturbances such as imbalances, harmonics, and frequency drifts, as well as to fulfill demanding grid code requirements and power quality standards. We also introduce a thorough output filter modeling and design, guidelines for the current reference calculation, computational time delay compensation, and discrete-time domain control description. A state observer is proposed to reduce the amount of sensors needed in the control stage; consequently, a simpler hardware, higher reliability, and lower cost implementation can be accomplished. Several tests, disturbances, and comparisons with other control approaches are performed to validate and illustrate the advantages of the control strategy.

Index Terms—Active damping, grid frequency variations, state estimation, voltage source converter (VSC), wind energy conversion system (WECS).

I. INTRODUCTION

A. Background

MANUFACTURERS' improvements in high-power switching devices, which can now individually manage up to 3.6 kA and 1.7 kV [1], facilitate that wind turbines based on full-converter topologies increase their rated power, becoming an attractive option in the market [2]. Full-power converter-based wind energy conversion systems (WECSs) can be implemented without gearbox (direct-drive scheme), which presents several advantages: the compact and simple design

with less moving parts decreases complexity and maintenance costs; frictional losses are reduced, and they are also more appropriate for large offshore generators.

The expected wind energy penetration levels and increasing number of high-power voltage source converters connected to the grid have generated concerns about harmonic-related issues. Power system operators are raising the power quality requirements and limiting the total harmonic distortion (THD) of the grid-injected current (see [3] and [4] for further details, and IEEE/IEC standard recommendations). Therefore, the reduction of harmonic injection is more relevant and the selection and design of the converter output filter become critical [5].

B. L versus LCL Output Filter

Inductance (L) filters present a simple design and control; however, for low-switching-frequency applications, the L filter requires a high value of inductance to fulfill the existing grid standards. In megawatt applications, a high value of the filter inductance becomes expensive and limits the bandwidth of the controller [6]–[8]. On the other hand, using inductance–capacitor–inductance (LCL) filters entails several advantages such as: to use relatively small inductor values; to reduce the output current THD; to diminish the size and cost of the output filter and to avoid compromising the bandwidth of the controller [8]–[11]. Nevertheless, the LCL filter requires the inclusion of a shunt capacitor bank and presents lightly damped oscillations at the LCL filter resonance.

C. Passive Versus Active Damping Strategies

There are two main approaches to reduce the lightly damped oscillations in an LCL filter: the passive and the active damping controls. The first one, by introducing a damping resistor in the LCL shunt branch, is able to increase the filter damping and to reduce the resonance peak [3], [4], [8]. This scheme presents a simple control strategy, since traditional L filter controllers can be used. However, in megawatt applications, the damping resistance required for a satisfactory performance usually results in high power losses and the inclusion of cooling systems which decrease the total WECS efficiency, turning the passive damping approach unacceptable or not practical [6], [12], [13]. In [14], a passive damping approach with reduced power losses is proposed. On the other hand, the active damping control, by implementing a controller which uses LCL filter information, allows us to mitigate the resonance without using any physical resistor [5]–[7], [13]–[20].

There are three techniques to achieve the active damping. One of them includes an additional internal loop into the controller using a measured or estimated state of the LCL filter (such as

Manuscript received September 18, 2012; revised December 08, 2012; accepted January 08, 2013. Date of publication February 01, 2013; date of current version June 17, 2013. This work was supported by Universidad Nacional del Sur, Consejo Nacional de Investigaciones Científicas y Técnicas (CONICET) and by Agencia Nacional de Promoción Científica y Tecnológica (ANPCyT), Argentina.

The authors are with Instituto de Investigaciones en Ingeniería Eléctrica (IIIE) “Alfredo Desages” (UNS-CONICET), Universidad Nacional del Sur (DIEC-UNS), Bahía Blanca 8000, Argentina (e-mail: aleon@ymail.com; jsolsona@uns.edu.ar).

Color versions of one or more of the figures in this paper are available online at <http://ieeexplore.ieee.org>.

Digital Object Identifier 10.1109/TSTE.2013.2239317

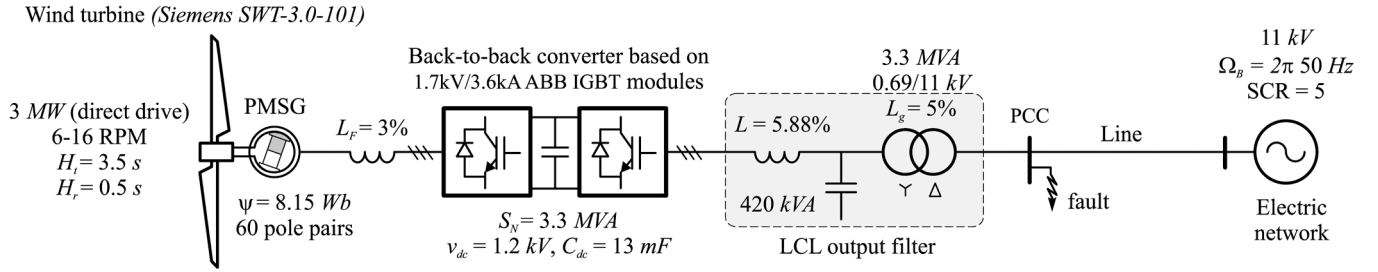


Fig. 1. Schematic representation of a variable-speed wind energy conversion system based on a direct-drive full-converter scheme.

capacitor current [6], [7], [21], capacitor voltage [5], [17], [18], [22], or converter-side current [13], [20]); another one uses a filter-based approach [12], [16] and in the remaining one, a full feedback of the LCL states is considered [14], [15], [19], [23], [24]. The last technique allows us to shape the closed-loop Bode plot placing all the eigenvalues in a predefined location and obtaining a higher performance.

D. Measurement Schemes

Some proposals introduce active damping controllers measuring all system states (converter- and grid-side currents and shunt capacitor voltage) [14], [15], [20]; however, this is not suitable for practical implementations, and measurement reduction is often preferred. Physical sensors can be replaced by software or virtual sensors based on state estimators to achieve a hardware simplification and higher reliability [24], [25]. In [5], [6], [22], open-loop estimators are used to obtain the capacitor and/or grid voltages. Closed-loop estimators based on the *Kalman* filter and *Luenberger* observer are also designed [9], [19], [21], [26] to improve the estimation performance of open-loop schemes. Different measures are estimated, such as: converter-side current and capacitor voltage [19]; capacitor voltage, grid-side current, and grid voltage [26]; capacitor voltage and capacitor current [9]; grid voltage [21], etc. In this way, additional sensors are avoided and the active damping approach can be implemented using the same measurements as a traditional L filter controller.

E. Unbalanced and Distorted Voltage Conditions

In order to achieve a proper operation of WECS converters, it is very important to consider grid disturbances in the control design stage to fulfill grid codes and to avoid a series of drawbacks which arise under distorted grid voltages. Under unbalanced conditions, the interaction of negative-sequence grid voltages with positive-sequence converter currents produces a sustained double grid frequency ($2\omega_g$) pulsation in the injected active power. This power pulsation also generates a $2\omega_g$ oscillation in the dc-bus voltage which can stress the switching devices and propagates the power pulsation to the turbine mechanical system. In addition, grid voltage harmonics distort the injected currents. As power quality standards demand a nearly harmonic-free current, both imbalances and harmonics must be properly addressed in the controller design.

F. Grid Frequency Variations

Active damping approaches are proposed in several works without considering imbalances and harmonics [5], [8], [11],

[14]–[20], [22] or grid frequency deviations [7], [9], [10], [26] in their controller designs; therefore, they are not fully appropriated for wind turbines connected to weak buses, or perform poorly when grid distortions arise at the connection point. On the other hand, approaches using resonant filters to reject harmonics can be susceptible to grid frequency drifts, particularly on those of higher resonance frequency. An appropriate control approach must be able to tune itself depending on the grid frequency.

To overcome the above drawbacks and to improve the wind turbine performance, we proposed a control structure which allows us to adapt the grid frequency involved in different control stages via a frequency-updating outer loop. Therefore, the grid-side converter control is tailored so that full-converter wind turbines inject a harmonic-free current even under severe harmonic distortions and frequency-varying conditions. In this way, wind farms can adequately fulfill demanding grid codes and power quality standards [27]. It will be shown that an LCL output filter controlled by an active damping approach and the proposed frequency-updating scheme results in a power quality improvement (lower THD in the output currents), especially in weak power networks subject to frequency variations.

II. FULL-POWER CONVERTER BASED WECS

A. Wind Turbine

The WECS considered is of a variable speed turbine and gearless type (direct-drive). The mechanical system is represented by a two-lumped-mass model. The electrical machine consists of a 3-MW permanent magnet generator, the parameters of which are taken from the *Siemens* wind turbine STW-3.0–101, and are included in Fig. 1 along with the WECS configuration and data.

B. Machine-Side Voltage Source Converter

The machine-side converter is an insulated gate bipolar transistor (IGBT)-based two-level converter connected through a filter to the generator stator. A rotating dq control aligned with the rotor position (d-axis) is chosen to control the stator currents. The reference current i_d^* is set to zero to avoid demagnetization, while the current i_q is used to regulate the dc-link voltage. The reference current i_q^* is calculated via a dc-voltage PI regulator plus a feed-forward term to minimize the dc voltage variations [28].

C. Grid-Side Voltage Source Converter

The grid-side converter is also an IGBT-based two-level converter connected to the grid via an LC filter and a step-up transformer. This converter manages the active and reactive powers injected by the full-converter wind turbine, and it will be developed in the following sections.

D. LCL Filter Modeling for the Control Design

1) *Model in the Continuous-Time Domain and Stationary $\alpha\beta$ Reference Frame:* Applying the Kirchhoff laws to the LCL filter circuit, the following model in a per-unit (p.u.) system results (see [11], [15], and [18]):

$$\frac{1}{\Omega_B} L \dot{\mathbf{i}}_{\alpha\beta} = -R \mathbf{i}_{\alpha\beta} - \mathbf{e}_{\alpha\beta} + \mathbf{v}_{\alpha\beta} \quad (1)$$

$$\frac{1}{\Omega_B} L_g \dot{\mathbf{i}}_{g\alpha\beta} = -R_g \mathbf{i}_{g\alpha\beta} - \mathbf{v}_{\alpha\beta} + \mathbf{v}_{g\alpha\beta} \quad (2)$$

$$\frac{1}{\Omega_B} C_t \dot{\mathbf{v}}_{\alpha\beta} = \mathbf{i}_{g\alpha\beta} - \mathbf{i}_{\alpha\beta} \quad (3)$$

where $\mathbf{i}_{\alpha\beta} = [i_\alpha \ i_\beta]^T$, $\mathbf{i}_{g\alpha\beta} = [i_{g\alpha} \ i_{g\beta}]^T$, and $\mathbf{v}_{\alpha\beta} = [v_\alpha \ v_\beta]^T$ are the converter-side current, grid-side current, and shunt branch voltage, respectively. The converter internal voltage is related to the duty cycle and the dc voltage by $\mathbf{e}_{\alpha\beta} = \boldsymbol{\eta}_{\alpha\beta} v_{dc}$. By choosing the state vector as

$$\mathbf{x} \triangleq [\mathbf{i}_{\alpha\beta} \ \mathbf{i}_{g\alpha\beta} \ \mathbf{v}_{\alpha\beta}]^T = [i_\alpha \ i_\beta \ i_{g\alpha} \ i_{g\beta} \ v_\alpha \ v_\beta]^T \quad (4)$$

a space-state representation of the LCL filter model (1)–(3) is given by

$$\dot{\mathbf{x}} = \mathbf{A}\mathbf{x} + \mathbf{B}\mathbf{e} + \mathbf{B}_g\mathbf{v} \quad (5)$$

where vectors $\mathbf{e}_{\alpha\beta}$ and $\mathbf{v}_{g\alpha\beta}$ are simply called \mathbf{e} and \mathbf{v} .

2) *Model in the Discrete-Time Domain and Stationary $\alpha\beta$ Reference Frame:* The system (5) can be digitized by using the zero-order hold (ZOH) discretization [29]. Therefore, in the discrete-time domain, the LCL filter model is represented as follows:

$$\mathbf{x}_{k+1} = \mathbf{A}'\mathbf{x}_k + \mathbf{B}'\mathbf{e}_k + \mathbf{B}_g'\mathbf{v}_k \quad (6)$$

where the discrete matrices are obtained from the continuous one as $\mathbf{A}' = e^{\mathbf{A}T_s}$, $\mathbf{B}' = \int_0^{T_s} e^{\mathbf{A}\tau} d\tau \mathbf{B}$ and $\mathbf{B}_g' = \int_0^{T_s} e^{\mathbf{A}\tau} d\tau \mathbf{B}_g$, being T_s the control sampling time.

3) *Model in the Discrete-Time Domain and Rotating dq Reference Frame:* The system (6) is transformed to a rotating dq reference frame in which the controller tuning of Section V will be easier. First, we introduce the discrete \mathcal{P} ark transformation at the sample times k and $k+1$

$$\mathbf{P}_k = \begin{bmatrix} \cos \theta_k & -\sin \theta_k \\ \sin \theta_k & \cos \theta_k \end{bmatrix} \quad (7)$$

$$\mathbf{P}_{k+1} = \begin{bmatrix} \cos \theta_{k+1} & -\sin \theta_{k+1} \\ \sin \theta_{k+1} & \cos \theta_{k+1} \end{bmatrix} \quad (8)$$

since the transformation rotates at the network angular speed, it verifies: $\theta_k = \omega_g t_k$ and $\theta_{k+1} = \omega_g t_{k+1} = \omega_g(t_k + T_s)$. Then, the transformations (7) and (8) allow us to define the matrix

$$\boldsymbol{\Omega} \triangleq \mathbf{P}_{k+1} \mathbf{P}_k^{-1} = \begin{bmatrix} \cos(\omega_g T_s) & -\sin(\omega_g T_s) \\ \sin(\omega_g T_s) & \cos(\omega_g T_s) \end{bmatrix}. \quad (9)$$

For a generic vector $\mathbf{f}^{\alpha\beta}$, it can be written $\mathbf{f}_k^{dq} = \mathbf{P}_k \mathbf{f}_k^{\alpha\beta}$ and $\mathbf{f}_{k+1}^{dq} = \mathbf{P}_{k+1} \mathbf{f}_{k+1}^{\alpha\beta}$; consequently, by applying the \mathcal{P} ark transformations (7) and (8) to the system (6), it results

$$\mathbf{P}_{k+1}^{-1} \mathbf{x}_{k+1}^{dq} = \mathbf{A}' \mathbf{P}_k^{-1} \mathbf{x}_k^{dq} + \mathbf{B}' \mathbf{P}_k^{-1} \mathbf{e}_k^{dq} + \mathbf{B}_g' \mathbf{P}_k^{-1} \mathbf{v}_k^{dq}. \quad (10)$$

Finally, premultiplying (10) by \mathbf{P}_{k+1} , the desired LCL filter model is obtained

$$\mathbf{x}_{k+1}^{dq} = \bar{\mathbf{A}} \mathbf{x}_k^{dq} + \bar{\mathbf{B}} \mathbf{e}_k^{dq} + \bar{\mathbf{B}}_g \mathbf{v}_k^{dq} \quad (11)$$

where the following matrices are defined $\bar{\mathbf{A}} \triangleq \mathbf{P}_{k+1} \mathbf{A}' \mathbf{P}_k^{-1}$, $\bar{\mathbf{B}} \triangleq \mathbf{P}_{k+1} \mathbf{B}' \mathbf{P}_k^{-1}$, and $\bar{\mathbf{B}}_g \triangleq \mathbf{P}_{k+1} \mathbf{B}_g' \mathbf{P}_k^{-1}$.

4) *Computational Time Delay Model:* The following equation, in the stationary $\alpha\beta$ reference frame, is introduced to consider the computational time delay

$$\mathbf{e}_{k+1} = \mathbf{u}_k. \quad (12)$$

This model represents a one-sample time delay which emphasizes that we cannot control the converter internal voltage \mathbf{e}_k while the measurement process is achieved at the sample k . We need to define an auxiliary control input \mathbf{u} which goes one-sample time behind ($\mathbf{e}_k = \mathbf{u}_{k-1}$). In this way, the controller takes into account the computational time delay, allowing a high bandwidth and avoiding stability problems. The discrete model (12) can be transformed to the rotating dq reference frame by using (7) and (8) and proceeding as in (11), yielding

$$\mathbf{e}_{k+1}^{dq} = \boldsymbol{\Omega} \mathbf{u}_k^{dq}. \quad (13)$$

III. LCL FILTER DESIGN

As LCL filter designs implemented in low-power and high-switching-frequency applications are not suitable for megawatt filters which use low switching frequencies [14], we will describe briefly the LCL filter design. Commercially available IGBT switches for megawatt applications present pulsewidth modulation (PWM) commutation frequencies up to a few kilohertz [1] (in our study, we assumed $f_{\text{pwm}} = 1.7$ kHz). As explained in [8], the LCL resonance frequency f_{res} has to be placed between ten times the grid frequency and one-half of the commutation frequency to avoid low- and high-frequency stability problems. Therefore, we set $f_{\text{res}} = (1/2)f_{\text{pwm}}$. To maximize the use of the existing WECS equipment, we proposed the step-up transformer inductance as the grid-side inductance of the LCL filter. In the per-unit system, a typical transformer inductance for this application is about 5%, so $L_g = 5\%$. To design the capacitance C_t of the shunt capacitor bank and the

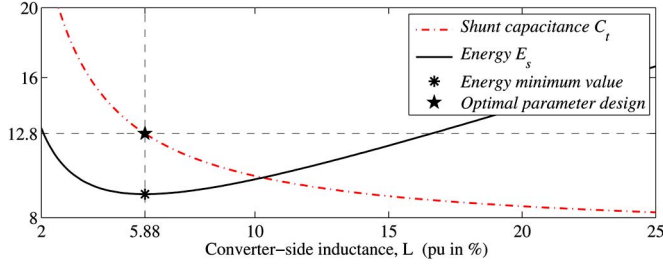


Fig. 2. Shunt capacitance C_t and energy E_s as a function of the converter-side inductance L (p.u. values in %).

converter-side inductance L , we used the LCL resonance frequency, which can be written as

$$f_{\text{res}} = \frac{\Omega_B}{2\pi} \sqrt{\frac{L_g + L}{L_g L C_t}} \quad (14)$$

then, it is possible to plot the value C_t as a function of the inductance L (see dotted-dashed line in Fig. 2). This curve presents the point pairs (L, C_t) which build all the LCL filters which have a $f_{\text{res}} = 1/2f_{\text{pwm}}$ and $L_g = 5\%$. In order to reduce the filter component size, we determined the optimal point by minimizing the stored energy which can be used as a relative measure of the size and weight of the filter [14]. The energy $E_s \triangleq 1/2LI_N^2 + 1/2C_tV_N^2$ in the per-unit system (in %) is presented with a solid line in Fig. 2. The minimum energy value is attained by a converter-side inductance of $L = 5.88\%$ (see asterisk mark in Fig. 2); consequently, a shunt capacitor bank of $C_t = 12.8\%$ (approximately 420 kVA) is considered.

IV. GRID-SIDE CURRENT REFERENCES

Several criteria to obtain the grid-side current references can be chosen under unbalanced conditions. We compared two schemes: the first one, called mode A, balances the ac-side currents at the expense of a $2\omega_g$ ripple on the dc voltage (i.e., nullifying negative-sequence currents $i_{gd}^- = i_{gq}^- = 0$); the second one, called mode B, eliminates the $2\omega_g$ ripple in the injected active power, and consequently reduces the $2\omega_g$ oscillations on the dc voltage, at the expense of an unbalanced ac-side current. How to obtain the grid-side current references in the mode-B case is described as follows.

The apparent power injected by the WECS to the grid can be written as [30], [31],

$$\begin{aligned} s_g = & (p_g + p_{gs} \sin 2\omega_g t + p_{gc} \cos 2\omega_g t) \\ & + j(q_g + q_{gs} \sin 2\omega_g t + q_{gc} \cos 2\omega_g t) \end{aligned} \quad (15)$$

where

$$p_g = i_{gd}^- v_{gd}^- + i_{gd}^+ v_{gd}^+ + i_{gq}^- v_{gq}^- + i_{gq}^+ v_{gq}^+ \quad (16)$$

$$q_g = i_{gq}^- v_{gd}^- + i_{gq}^+ v_{gd}^+ - i_{gd}^- v_{gq}^- - i_{gd}^+ v_{gq}^+ \quad (17)$$

$$p_{gs} = i_{gq}^+ v_{gd}^- - i_{gq}^- v_{gd}^+ - i_{gd}^+ v_{gq}^- + i_{gd}^- v_{gq}^+ \quad (18)$$

$$p_{gc} = i_{gd}^+ v_{gd}^- + i_{gd}^- v_{gd}^+ + i_{gq}^+ v_{gq}^- + i_{gq}^- v_{gq}^+ \quad (19)$$

p_g and q_g are the constant components of the active and reactive powers, whereas p_{gs} and p_{gc} are the amplitude of the sine and cosine $2\omega_g$ oscillation terms of active power, which arise under unbalanced voltages (see [28] and [30] for further details). In order to eliminate the $2\omega_g$ ripple in the injected active power, its oscillating terms must be nullified ($p_{gs} = p_{gc} = 0$). On the other hand, the reference of the WECS active power p_g is obtained from a maximum power point tracking (MPPT) algorithm. The reference of the injected reactive power q_g is calculated from a grid code curve which relates the injection of reactive current with the voltage amplitude at the point of common coupling (PCC) [32], [33]. Therefore, from (16)–(19), the grid-side current references are obtained as

$$i_{gd}^{+*} = (p_g^+ v_{gd}^+ \Delta_1 - q_g^+ v_{gq}^+ \Delta_2) (\Delta_1 \Delta_2)^{-1} \quad (20)$$

$$i_{gq}^{+*} = (p_g^+ v_{gq}^+ \Delta_1 + q_g^+ v_{gd}^+ \Delta_2) (\Delta_1 \Delta_2)^{-1} \quad (21)$$

$$i_{gd}^{-*} = (-p_g^- v_{gd}^- \Delta_1 - q_g^- v_{gq}^- \Delta_2) (\Delta_1 \Delta_2)^{-1} \quad (22)$$

$$i_{gq}^{-*} = (-p_g^- v_{gq}^- \Delta_1 + q_g^- v_{gd}^- \Delta_2) (\Delta_1 \Delta_2)^{-1} \quad (23)$$

where symbols $(+)$, $(-)$, and $(*)$ are used to indicate a positive sequence, negative sequence and reference value, respectively. Whereas, it was defined $\Delta_1 \triangleq v_{gd}^{+2} + v_{gq}^{+2} + v_{gd}^{-2} + v_{gq}^{-2}$ and $\Delta_2 \triangleq v_{gd}^{+2} + v_{gq}^{+2} - v_{gd}^{-2} - v_{gq}^{-2}$. A block diagram describing the reference calculation stage is shown in Fig. 3. The required detection of the positive and negative sequence voltages under distorted conditions is accomplished by using the technique described in [34].

V. CONTROLLER DESIGN

A. Dynamic Extension of the System

The grid-side converter must manage its output current fast and accurately to meet grid-code fault-ride-through requirements under balanced conditions; it must also be able to control the negative-sequence current under unbalanced conditions (following the current references calculated in the above section); additionally, when harmonics arise in the PCC voltage, the WECS must keep an output current with a THD of less than 5% to fulfill the power quality standards (e.g., see IEEE 1547-2003 standard requirement). In a reference frame rotating to the grid angular speed ω_g , the above specifications can be met as follows: first, a PI controller is implemented to track constant components ($+\omega_g$ frequency in the stationary $\alpha\beta$ reference frame, balanced condition); second, a resonant filter with resonant frequency at $2\omega_g$ is added to make a high gain path in the controller, guaranteeing a null steady-state error for $2\omega_g$ components in the current references ($-\omega_g$ frequency, unbalanced condition); third, resonant filters with resonant frequencies at $6\omega_g$ (harmonics $-5\omega_g$ and $+7\omega_g$), $12\omega_g$ (harmonics $-11\omega_g$ and $+13\omega_g$), and so on are included to allow WECS to inject sinusoidal currents under distorted conditions.

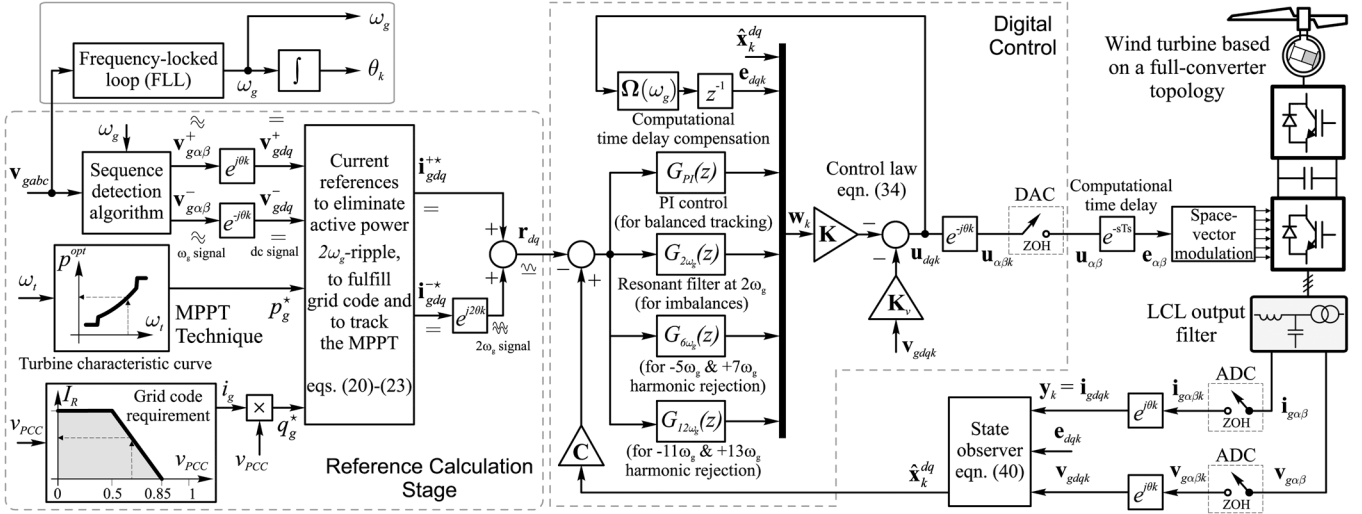


Fig. 3. Block diagram of the proposed control strategy.

A procedure to extend the system including the above elements is introduced as follows. To build the PI regulator, an integrator can be represented in the discrete-time domain as

$$\eta_{k+1} = \eta_k + T_s s_k \quad (24)$$

where $s_k = \mathbf{C}\mathbf{x}_k^{dq} - \mathbf{r}_k^{dq}$ indicates the tracking error of the grid-side current, \mathbf{r}_k^{dq} is the reference current vector, and the following output matrix is chosen [see (4)]:

$$\mathbf{C} \triangleq \begin{bmatrix} 0 & 0 & 1 & 0 & 0 & 0 \\ 0 & 0 & 0 & 1 & 0 & 0 \end{bmatrix}. \quad (25)$$

On the other hand, in the continuous-time domain, a resonant filter with resonant frequency ω_r , is given by

$$G_r(s) = \frac{s}{s^2 + \omega_r^2}. \quad (26)$$

The continuous transfer function of two resonant filters (one for the d-axis and another for the q-axis component) can be digitized using the ZOH discretization and written in a state-space representation as [29]

$$\mathbf{h}_{k+1}^{\omega_r} = \mathbf{A}^{\omega_r} \mathbf{h}_k^{\omega_r} + \mathbf{B}^{\omega_r} \mathbf{s}_k. \quad (27)$$

By combining the system model (11), computational time delay model (13), PI integrators (24), and resonant filters at frequencies $2\omega_g$, $6\omega_g$, and $12\omega_g$ [using the resonant model (27)], the system can be extended to

$$\mathbf{w}_{k+1} = \mathbf{A}_e \mathbf{w}_k + \mathbf{B}_e \mathbf{u}_k^{dq} + \mathbf{B}_{ge} \mathbf{v}_k^{dq} - \mathbf{B}_{re} \mathbf{r}_k^{dq} \quad (28)$$

where an extended state vector \mathbf{w}_k is defined, along with the following extended matrices:

$$\mathbf{w}_k \triangleq [\mathbf{x}_k^{dq} \quad \mathbf{e}_k^{dq} \quad \eta_k \quad \mathbf{h}_k^{\omega_2} \quad \mathbf{h}_k^{\omega_6} \quad \mathbf{h}_k^{\omega_{12}}]^T \quad (29)$$

$$\mathbf{A}_e \triangleq \begin{bmatrix} \bar{\mathbf{A}} & \bar{\mathbf{B}} & \mathbf{0} & \mathbf{0} & \mathbf{0} & \mathbf{0} \\ \mathbf{0} & \mathbf{0} & \mathbf{0} & \mathbf{0} & \mathbf{0} & \mathbf{0} \\ T_s \mathbf{C} & \mathbf{0} & \mathbf{I} & \mathbf{0} & \mathbf{0} & \mathbf{0} \\ \mathbf{B}^{\omega_2} \mathbf{C} & \mathbf{0} & \mathbf{0} & \mathbf{A}^{\omega_2} & \mathbf{0} & \mathbf{0} \\ \mathbf{B}^{\omega_6} \mathbf{C} & \mathbf{0} & \mathbf{0} & \mathbf{0} & \mathbf{A}^{\omega_6} & \mathbf{0} \\ \mathbf{B}^{\omega_{12}} \mathbf{C} & \mathbf{0} & \mathbf{0} & \mathbf{0} & \mathbf{0} & \mathbf{A}^{\omega_{12}} \end{bmatrix} \quad (30)$$

$$\mathbf{B}_e \triangleq [\mathbf{0} \quad \boldsymbol{\Omega} \quad \mathbf{0} \quad \mathbf{0} \quad \mathbf{0} \quad \mathbf{0}]^T \quad (31)$$

$$\mathbf{B}_{ge} \triangleq [\bar{\mathbf{B}}_g \quad \mathbf{0} \quad \mathbf{0} \quad \mathbf{0} \quad \mathbf{0} \quad \mathbf{0}]^T \quad (32)$$

$$\mathbf{B}_{re} \triangleq [\mathbf{0} \quad \mathbf{0} \quad T_s \mathbf{I} \quad \mathbf{B}^{\omega_2} \quad \mathbf{0} \quad \mathbf{0}]^T. \quad (33)$$

B. Control Law Design Using the State-Space Approach

The control law \mathbf{u}_k^{dq} is obtained feeding back the extended states plus a feed-forward term to reduce grid voltage variations [13], [15]. Therefore,

$$\mathbf{u}_k^{dq} = -\mathbf{K} \mathbf{w}_k - \mathbf{K}_v \mathbf{v}_k^{dq}. \quad (34)$$

By substituting the control law (34) in the extended system (28), the closed-loop system is given by

$$\mathbf{w}_{k+1} = (\mathbf{A}_e - \mathbf{B}_e \mathbf{K}) \mathbf{w}_k + (\mathbf{B}_{ge} - \mathbf{B}_e \mathbf{K}_v) \mathbf{v}_k^{dq} - \mathbf{B}_{re} \mathbf{r}_k^{dq}.$$

Finally, the feedback gain matrix \mathbf{K} is chosen so that the closed-loop matrix $(\mathbf{A}_e - \mathbf{B}_e \mathbf{K})$ has all its eigenvalues in a desired location. This can be made by using the optimal quadratic regulation [29] which, by minimizing the cost function $J = \sum_{k=1}^{\infty} (\mathbf{w}_k^T \mathbf{Q} \mathbf{w}_k + \mathbf{u}_k^T \mathbf{R} \mathbf{u}_k)$, obtains the optimal control gain \mathbf{K} .

C. Grid Frequency Adaptation

In electrical networks with negligible frequency variations, the LCL-filter control strategy can be implemented without updating the grid frequency in the control algorithm. However, in weak networks where the grid frequency can have some deviation, it is important to consider this variation in the control design stage; otherwise, the harmonic rejection capability can be

reduced. In order to improve the control performance, we proposed an outer loop which updates the grid frequency in the rotating dq reference frame, resonant filters, and sequence detection algorithm. Thus, the performance and operation of full-converter wind turbines are enhanced; namely, negative-sequence currents are controlled under imbalances, harmonic-free currents are injected under distorted conditions, and a self-tuning feature is attained under grid frequency drifts. To obtain the grid frequency, we implemented the frequency-locked loop (FLL) technique described in [35]. A block diagram of the whole proposed control strategy implementation is presented in Fig. 3.

VI. REDUCTION OF THE MEASUREMENTS

The control law developed in the previous section requires the measurement of the converter- and grid-side currents (\mathbf{i} , \mathbf{i}_g) as well as the shunt branch voltage (\mathbf{v}). In this section, a state observer (software sensor) is developed to reduce the amount of sensors. The dynamics of the LCL filter system (11) can be rewritten as

$$\mathbf{x}_k^{dq} = \bar{\mathbf{A}}\mathbf{x}_{k-1}^{dq} + \mathbf{d}_{k-1} \quad (35)$$

$$\mathbf{y}_{k-1} = \mathbf{C}\mathbf{x}_{k-1}^{dq} \quad (36)$$

where the auxiliary vector $\mathbf{d}_{k-1} \triangleq \bar{\mathbf{B}}\mathbf{e}_{k-1}^{dq} + \bar{\mathbf{B}}_g\mathbf{v}_{k-1}^{dq}$ is defined. The vector $\mathbf{y} = \mathbf{i}_g^{dq}$ is the measured state (grid-side current), and the estimated states are the converter-side current and shunt branch voltage. To accomplish the desired state estimation, a conventional prediction-type *Luenberger* observer can be implemented, using the system (35), (36) as follows:

$$\hat{\mathbf{x}}_k^{dq} = \bar{\mathbf{A}}\hat{\mathbf{x}}_{k-1}^{dq} + \mathbf{d}_{k-1} + \mathbf{G}(\mathbf{y}_{k-1} - \mathbf{C}\hat{\mathbf{x}}_{k-1}^{dq}) \quad (37)$$

where the symbol $(\hat{\cdot})$ indicates an estimated value, and the gain matrix $\mathbf{G} \in \mathbb{R}^{6 \times 2}$ should be chosen to guarantee that the estimation error converges to zero. However, in the prediction-type observer, the estimated state $\hat{\mathbf{x}}_k^{dq}$ is obtained from measurements of the output vector up to \mathbf{y}_{k-1} ; consequently, the estimation algorithm does not use the information of the current output \mathbf{y}_k . On the other hand, a different approach called filtering-type observer allows us to use the information \mathbf{y}_k to estimate $\hat{\mathbf{x}}_k^{dq}$. This algorithm can be synthesized by the following equations [29]:

$$\hat{\mathbf{x}}_k^{dq} = \bar{\mathbf{A}}\hat{\mathbf{x}}_{k-1}^{dq} + \mathbf{d}_{k-1} + \mathbf{G}(\mathbf{y}_k - \hat{\mathbf{y}}_k) \quad (38)$$

$$\hat{\mathbf{y}}_k = \mathbf{C}\hat{\mathbf{x}}_k^{dq} = \mathbf{C}(\bar{\mathbf{A}}\hat{\mathbf{x}}_{k-1}^{dq} + \mathbf{d}_{k-1}). \quad (39)$$

By combining (38) and (39), the filtering-type observer structure can be simplified as follows:

$$\hat{\mathbf{x}}_k^{dq} = (\mathbf{I} - \mathbf{G}\mathbf{C})(\bar{\mathbf{A}}\hat{\mathbf{x}}_{k-1}^{dq} + \mathbf{d}_{k-1}) + \mathbf{G}\mathbf{y}_k. \quad (40)$$

To find the \mathbf{G} matrix first, we defined the estimation error as $\tilde{\mathbf{x}}_k^{dq} \triangleq \mathbf{x}_k^{dq} - \hat{\mathbf{x}}_k^{dq}$, and obtained the estimation error dynamics by subtracting (40) from (35), hence,

$$\tilde{\mathbf{x}}_k^{dq} = (\bar{\mathbf{A}} - \mathbf{G}\mathbf{C}\bar{\mathbf{A}})\tilde{\mathbf{x}}_{k-1}^{dq}. \quad (41)$$

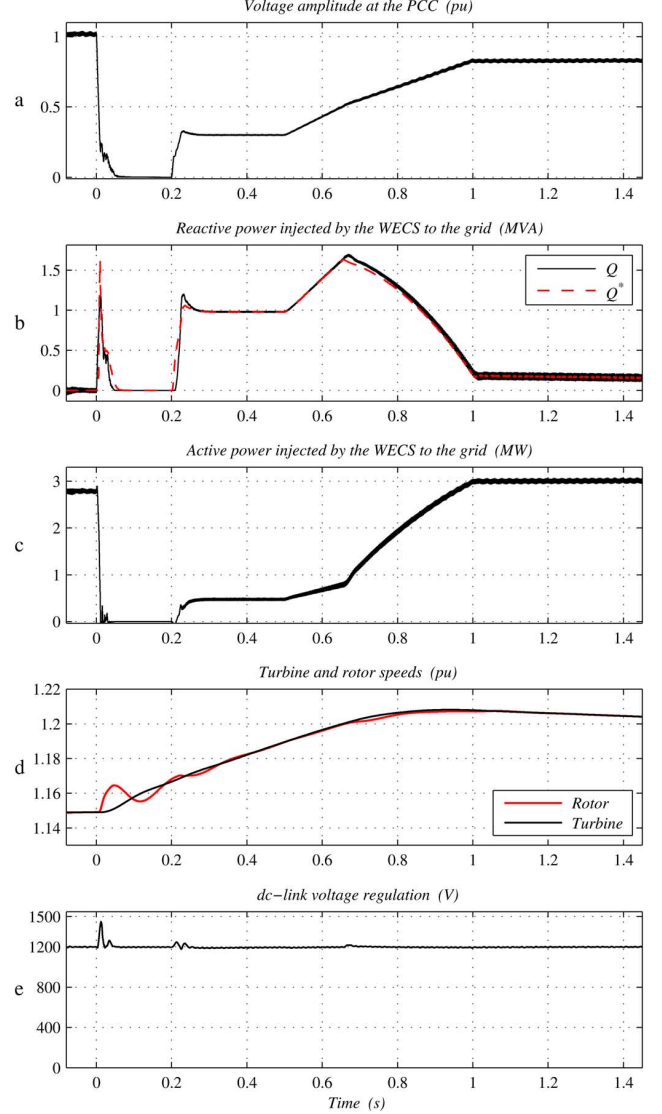


Fig. 4. Three-phase fault test and behavior of the main WECS variables.

Finally, the matrix \mathbf{G} is designed using matrix techniques such as eigenvalue placement or the optimal quadratic approach (the latter is used in our design). Thereby, the matrix $(\bar{\mathbf{A}} - \mathbf{G}\mathbf{C}\bar{\mathbf{A}})$ presents stable eigenvalues, and the estimation error converges to zero with a desired rate.

VII. PERFORMANCE TESTING

The WECS configuration, LCL filter, digital controller and data used in the tests are shown in Figs. 1 and 3. The PWM switching frequency is $f_{\text{pwm}} = 1700$ Hz, and the sampling frequency is $f_s = 3400$ Hz (i.e., a sampling time of $T_s = 294 \mu\text{s}$).

A. Fault Ride-Through Capability and Reactive Power Control

A three-phase fault test was performed to evaluate the fault ride-through capability and the grid code fulfillment. The fault voltage sag was taken from the Spanish grid code, with a more severe 150-ms zero voltage sag at the beginning of the fault [see Fig. 4(a)]. Grid codes demand WECSs not only to remain

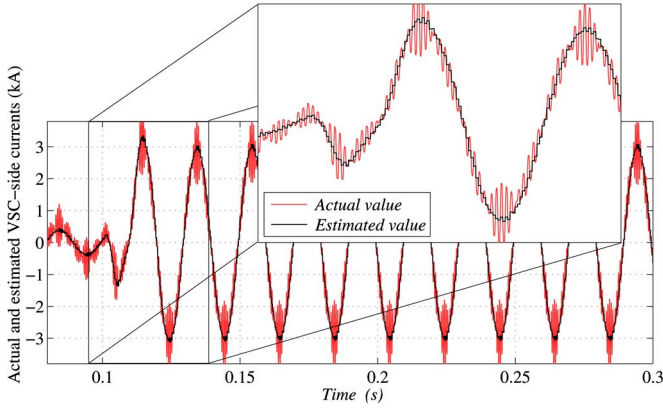


Fig. 5. Transient and steady-state behavior of the observer. A-phase of the actual and estimated converter-side current.

connected under these voltage sags but also to deliver reactive current to support the grid voltage recovery. The reactive power required by the grid code (dashed line Q^*) and the injected reactive power by the WECS (solid line Q) are plotted in Fig. 4(b) which shows that the proposed controller has more than enough bandwidth to ride-through the severe fault, and to properly meet the grid code requirement. The active power injected by the WECS is also given in Fig. 4(c). Because the low voltage condition does not allow us to export all the wind mechanical power, there is an increase in the turbine and rotor speeds [see Fig. 4(d)]. However, the speeds remain inside the operating variable-speed range of the WECS and, after the fault, the speeds gradually return to its optimal value (not shown in the figure). Finally, Fig. 4(e) presents the dc-link voltage regulation during the fault period, showing a good performance considering the extreme test.

The state observer was tested during a step reference in the injected current. Fig. 5 shows the transient and steady-state behavior of the actual and estimated converter-side current. The observer is able to fast and properly estimate the states without phase error. The 1.7-kHz commutation ripple is clearly observed in the actual current; however, an additional advantage is provided by the observer, since its filter action reduces the commutation ripple and sensor measurement noises.

B. Asymmetrical Test

A test involving an unbalanced grid voltage was considered. This imbalance could be generated by a large unbalanced load, or may arise during a grid asymmetrical fault. The imbalance, with an unbalanced factor of 31%, takes place at $t = 0.05$ s and then at $t = 0.25$ s, is cleared [see Fig. 6(a)]. To compute the current references during the asymmetrical fault, both modes A and B of Section IV were implemented [see Fig. 6(c)]. The current injected to the grid with both modes is presented in Fig. 6(b). Fig. 6(c) shows that, when the mode A is used, after the beginning of the imbalance at $t = 0.05$ s, a nonnegligible $2\omega_g$ pulsation arises in the active power injected by the WECS to the grid. However, at $t = 0.15$ s, when switching to mode B, this power pulsation is completely nullified, and the $2\omega_g$ ripple on the dc-link voltage is also reduced [see Fig. 6(d)]. Consequently, a constant injected power under unbalanced conditions

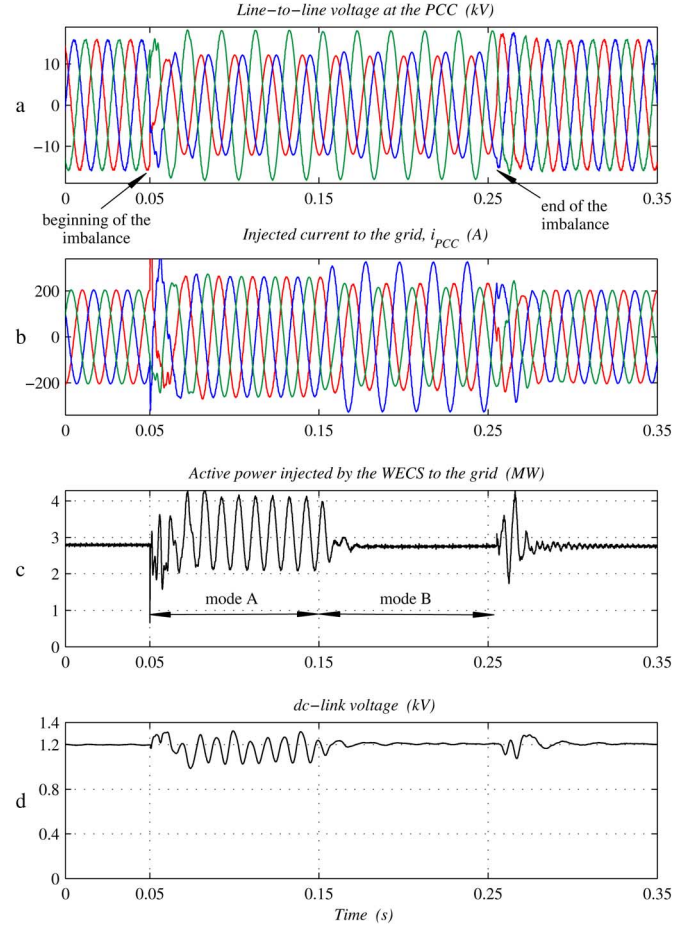


Fig. 6. Test with an unbalanced grid voltage.

is attained, and switching device and mechanical system stress are decreased as well.

C. Harmonic Rejection and Grid Frequency Adaptation

A last test was introduced to analyze the controller performance when harmonics and frequency variations are present in the electric network. First, to obtain a distorted voltage waveform, harmonics are added at $t = 0.04$ s [see Fig. 7(a)]; then, a grid frequency step of -0.75 Hz is performed at $t = 0.13$ s. Three control strategies were compared: *i*) a controller without neither harmonic rejection nor frequency adaptation [Fig. 7(b)]; *ii*) a conventional controller based on resonant filters [Fig. 7(c)]; and *iii*) the proposed controller with disturbance rejection and frequency adaptation [Fig. 7(d)]. Fig. 7(b) shows that, when using the controller *i*, there is a high distortion in the injected currents after $t = 0.04$ s, due to the high distorted grid voltage and the relatively low output filter inductance. The controller *ii* can attenuate the current harmonics in Sector B (time interval 0.04 s–0.13 s) but, after the grid frequency variation at $t = 0.13$ s, the current THD increases to 6.38%. Finally, Fig. 7(d) presents the performance of the proposed control algorithm, where the injected currents are almost harmonic-free (THD below 1%) for both grid disturbances: voltage harmonics and frequency deviations. We also included on the right-side of Fig. 7, the harmonic spectra and THD of the PCC voltage and grid-injected currents, after both

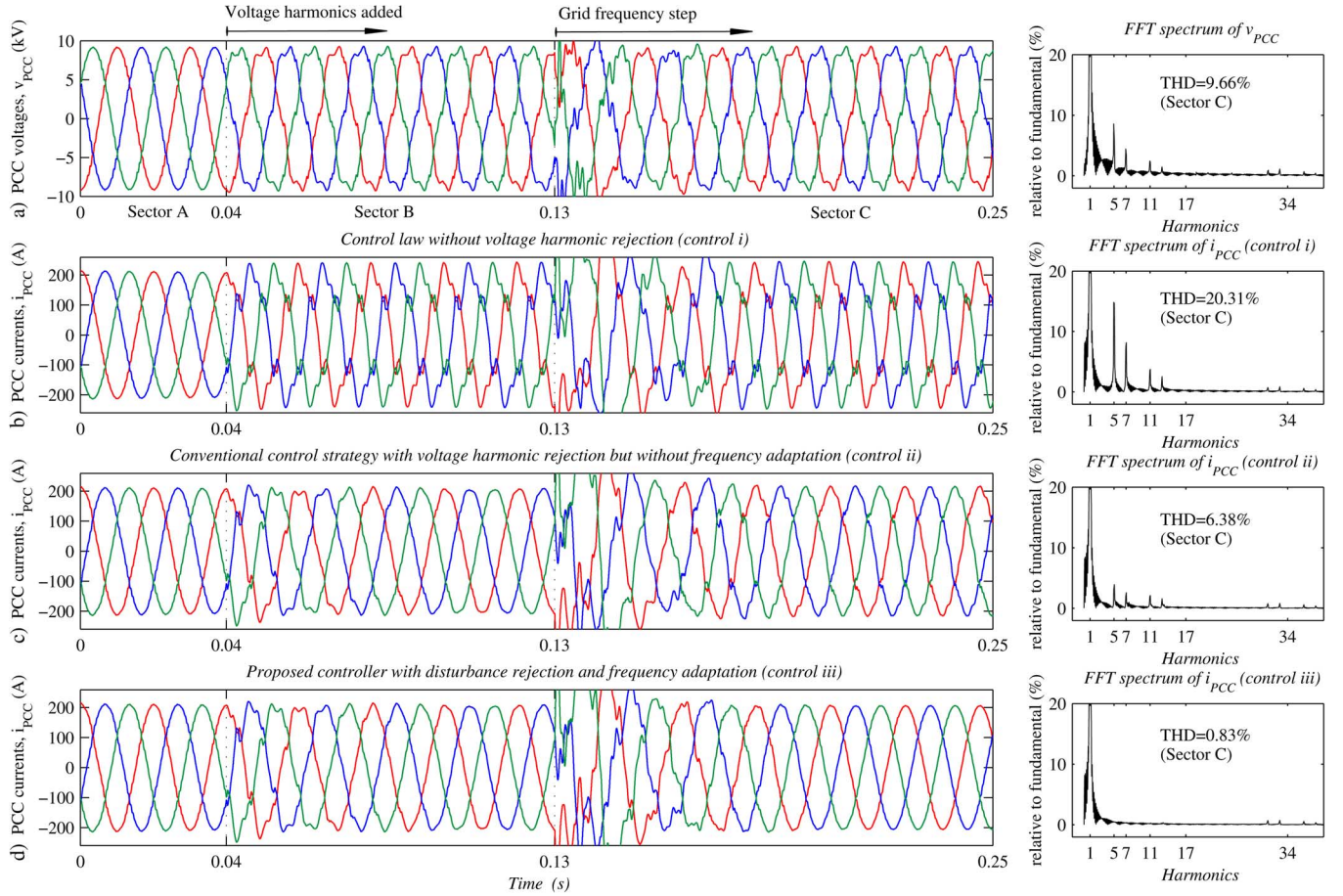


Fig. 7. Harmonic rejection capability and grid frequency adaptation of three different control strategies.

grid disturbances took place (time interval named Sector C in Fig. 7). There, the power quality improvement of the proposed strategy under distorted grid conditions is shown.

VIII. CONCLUSION

The operation of full-converter wind turbines under imbalances, harmonics, and frequency deviations was enhanced by means of an *LCL* output filter controlled by an improved active damping scheme. Unlike other *LCL*-filter controllers which are only focused on the *LCL* resonance damping, the proposed controller addressed, in the control design stage, both the *LCL* resonance damping and most grid disturbances which can arise in weak power networks. Below, there is a summary of the main features of the proposal.

- 1) The harmonic rejection capability of the wind turbine grid-side converter was improved, even under frequency-varying conditions.
- 2) A state observer was designed to reduce the amount of sensors, and consequently to accomplish a simpler hardware, higher reliability, and lower cost implementation.
- 3) A large fault ride-through capability was achieved, as well as an accurate reactive power control required by grid codes.
- 4) The $2\omega_g$ pulsations in the injected active power and dc-link voltage were reduced under unbalanced conditions.

- 5) A discrete-time domain design considering the computational time delay permitted a high bandwidth controller and easier digital signal processor implementation.

REFERENCES

- [1] M. Rahimo, D. Schneider, R. Schnell, S. Eicher, and U. Schlappbach, "Hipak Modules With SPT + Technology Rated up to 3.6 kA," in *Proc. PCIM Eur. Conf. 2006*, Nuremberg, Germany, pp. 1–5, ABB Technical publication.
- [2] H. Geng and D. Xu, "Stability analysis and improvements for variable-speed multipole permanent magnet synchronous generator-based wind energy conversion system," *IEEE Trans. Sustain. Energy*, vol. 2, no. 4, pp. 459–467, Oct. 2011.
- [3] S. Araujo, A. Engler, B. Sahan, and F. Antunes, "LCL filter design for grid-connected NPC inverters in offshore wind turbines," in *Proc. 7th Int. Conf. Power Electr. (ICPE'07)*, Oct. 2007, pp. 1133–1138.
- [4] A. Rockhill, M. Liserre, R. Teodorescu, and P. Rodriguez, "Grid-filter design for a multimewatt medium-voltage voltage-source inverter," *IEEE Trans. Ind. Electron.*, vol. 58, no. 4, pp. 1205–1217, Apr. 2011.
- [5] M. Malinowski and S. Bernet, "A simple voltage sensorless active damping scheme for three-phase PWM converters with an LCL filter," *IEEE Trans. Ind. Electron.*, vol. 55, no. 4, pp. 1876–1880, Apr. 2008.
- [6] L. A. Serpa, S. Ponnaluri, P. M. Barbosa, and J. W. Kolar, "A modified direct power control strategy allowing the connection of three-phase inverters to the grid through LCL filters," *IEEE Trans. Ind. Appl.*, vol. 43, no. 5, pp. 1388–1400, Sep./Oct. 2007.
- [7] E. Twining and D. Holmes, "Grid current regulation of a three-phase voltage source inverter with an LCL input filter," *IEEE Trans. Power Electron.*, vol. 18, no. 3, pp. 888–895, May 2003.
- [8] M. Liserre, F. Blaabjerg, and S. Hansen, "Design and control of an LCL-filter-based three-phase active rectifier," *IEEE Trans. Ind. Appl.*, vol. 41, no. 5, pp. 1281–1291, Sep./Oct. 2005.

- [9] S. Mariethoz and M. Morari, "Explicit model-predictive control of a PWM inverter with an LCL filter," *IEEE Trans. Ind. Electron.*, vol. 56, no. 2, pp. 389–399, Feb. 2009.
- [10] Y. Tang, P. C. Loh, P. Wang, F. H. Choo, and F. Gao, "Exploring inherent damping characteristic of LCL-filters for three-phase grid-connected voltage source inverters," *IEEE Trans. Power Electron.*, vol. 27, no. 3, pp. 1433–1443, Mar. 2012.
- [11] S. Khajehoddin, M. Karimi-Ghartemani, P. Jain, and A. Bakhshai, "A control design approach for three-phase grid-connected renewable energy resources," *IEEE Trans. Sustain. Energy*, vol. 2, no. 4, pp. 423–432, Oct. 2011.
- [12] M. Liserre, R. Teodorescu, and F. Blaabjerg, "Stability of photovoltaic and wind turbine grid-connected inverters for a large set of grid impedance values," *IEEE Trans. Power Electron.*, vol. 21, no. 1, pp. 263–272, Jan. 2006.
- [13] G. Shen, X. Zhu, J. Zhang, and D. Xu, "A new feedback method for PR current control of LCL-filter-based grid-connected inverter," *IEEE Trans. Ind. Electron.*, vol. 57, no. 6, pp. 2033–2041, Jun. 2010.
- [14] F. A. Magueed and J. Svensson, "Control of VSC connected to the grid through LCL-filter to achieve balanced currents," in *Proc. 40th IAS Ann. Meeting IEEE Ind. Appl. Conf.*, Oct. 2005, vol. 1, pp. 572–578.
- [15] E. Wu and P. W. Lehn, "Digital current control of a voltage source converter with active damping of LCL resonance," *IEEE Trans. Power Electron.*, vol. 21, no. 5, pp. 1364–1373, Sep. 2006.
- [16] M. Liserre, A. Dell'Aquila, and F. Blaabjerg, "Genetic algorithm-based design of the active damping for an LCL-filter three-phase active rectifier," *IEEE Trans. Power Electron.*, vol. 19, no. 1, pp. 76–86, Jan. 2004.
- [17] P. A. Dahono, "A control method to damp oscillation in the input LC filter of AC-DC PWM converters," in *Proc. IEEE 33rd Annual Power Electronics Specialists Conf. (PESC'02)*, Jun. 2002, vol. 4, pp. 1630–1635.
- [18] V. Blasko and V. Kaura, "A novel control to actively damp resonance in input LC filter of a three-phase voltage source converter," *IEEE Trans. Ind. Appl.*, vol. 33, no. 2, pp. 542–550, Mar./Apr. 1997.
- [19] F. Huerta, E. Bueno, S. Cobrecas, F. Rodriguez, and C. Giron, "Control of grid-connected voltage source converters with LCL filter using a linear quadratic servocontroller with state estimator," in *Proc. IEEE Power Electronics Specialists Conf. (PESC'08)*, Jun. 2008, pp. 3794–3800.
- [20] M. Bongiorno and J. Svensson, "Voltage dip mitigation using shunt-connected voltage source converter," *IEEE Trans. Power Electron.*, vol. 22, no. 5, pp. 1867–1874, Sep. 2007.
- [21] Y. A.-R. I. Mohamed, M. A.-Rahman, and R. Seethapathy, "Robust line-voltage sensorless control and synchronization of LCL-filtered distributed generation inverters for high power quality grid connection," *IEEE Trans. Power Electron.*, vol. 27, no. 1, pp. 87–98, Jan. 2012.
- [22] M. Malinowski, S. Stynski, W. Kolomyjski, and M. Kazmierkowski, "Control of three-level PWM converter applied to variable-speed-type turbines," *IEEE Trans. Ind. Electron.*, vol. 56, no. 1, pp. 69–77, Jan. 2009.
- [23] A. Draou, Y. Sato, and T. Kataoka, "A new state feedback based transient control of PWM AC to DC voltage type converters," *IEEE Trans. Power Electron.*, vol. 10, no. 6, pp. 716–724, Nov. 1995.
- [24] B. Halimi and P. Dahono, "A current control method for phase-controlled rectifier that has an LCL filter," in *Proc. IEEE Inter. Conf. Power Electr. and Drive Systems*, Oct. 2001, vol. 1, pp. 20–25.
- [25] A. E. Leon, J. M. Mauricio, J. A. Solsona, and A. Gomez-Exposito, "Software sensor-based STATCOM control under unbalanced conditions," *IEEE Trans. Power Del.*, vol. 24, no. 3, pp. 1623–1632, Jul. 2009.
- [26] B. Bolsens, K. De Brabandere, J. Van den Keybus, J. Driesen, and R. Belmans, "Model-based generation of low distortion currents in grid-coupled PWM-inverters using an LCL output filter," *IEEE Trans. Power Electron.*, vol. 21, no. 4, pp. 1032–1040, Jul. 2006.
- [27] M. Tsili and S. Papathanassiou, "A review of grid code technical requirements for wind farms," *IET Renew. Power Generat.*, vol. 3, pp. 308–332, Sep. 2009.
- [28] A. E. Leon, J. M. Mauricio, J. A. Solsona, and A. Gomez-Exposito, "Adaptive control strategy for VSC-based systems under unbalanced network conditions," *IEEE Trans. Smart Grid*, vol. 1, no. 3, pp. 311–319, Dec. 2010.
- [29] K. Ogata, *Discrete-Time Control Systems*, 2nd ed. Englewood Cliffs, NJ, USA: Prentice-Hall, 1995.
- [30] S. Chaudhary, R. Teodorescu, P. Rodriguez, P. Kjaer, and A. Gole, "Negative sequence current control in wind power plants with VSC-HVDC connection," *IEEE Trans. Sustain. Energy*, vol. 3, no. 3, pp. 535–544, Jul. 2012.
- [31] A. E. Leon, J. M. Mauricio, and J. A. Solsona, "Fault ride-through enhancement of DFIG-based wind generation considering unbalanced and distorted conditions," *IEEE Trans. Energy Convers.*, vol. 27, no. 3, pp. 775–783, Sep. 2012.
- [32] S. De Rijcke, H. Ergun, D. Van Hertem, and J. Driesen, "Grid impact of voltage control and reactive power support by wind turbines equipped with direct-drive synchronous machines," *IEEE Trans. Sustain. Energy*, vol. 3, no. 4, pp. 890–898, Oct. 2012.
- [33] A. E. Leon, J. M. Mauricio, A. Gomez-Exposito, and J. A. Solsona, "An improved control strategy for hybrid wind farms," *IEEE Trans. Sustain. Energy*, vol. 1, no. 3, pp. 131–141, Oct. 2010.
- [34] K. Selvajothi and P. A. Janakiraman, "Extraction of harmonics using composite observers," *IEEE Trans. Power Del.*, vol. 23, no. 1, pp. 31–40, Jan. 2008.
- [35] P. Rodriguez, A. Luna, R. Muñoz-Aguilar, I. Etxeberria-Otadui, R. Teodorescu, and F. Blaabjerg, "A stationary reference frame grid synchronization system for three-phase grid-connected power converters under adverse grid conditions," *IEEE Trans. Power Electron.*, vol. 27, no. 1, pp. 99–112, Jan. 2012.



Andres E. Leon (S'05–M'13) was born in Argentina, in 1979. He received the Electrical Engineering degree from the Universidad Nacional del Comahue, Neuquén, Argentina, and the Ph.D. degree from the Universidad Nacional del Sur, Bahía Blanca, Argentina, in 2005 and 2011, respectively.

He is currently working at the Instituto de Investigaciones en Ingeniería Eléctrica "Alfredo Desages" (IIIE-CONICET), Bahía Blanca, Argentina. His primary areas of interest are power system control and wind energy conversion systems.



Jorge A. Solsona (SM'04) received the electronics engineer and Ph.D. degrees from the Universidad Nacional de La Plata, La Plata, Argentina, in 1986 and 1995, respectively.

Currently, he is with the Instituto de Investigaciones en Ingeniería Eléctrica Alfredo Desages (IIIE), Departamento de Ingeniería Eléctrica y de Computadoras, Universidad Nacional del Sur, Bahía Blanca, Argentina, and CONICET where he is involved in teaching and research on control theory and its applications to electromechanical systems.